

JGR Solid Earth

RESEARCH ARTICLE

10.1029/2022JB024488

Key Points:

- Dynamic ring shear tests show the deformation characteristics of granular materials under vibration
- Longer durations and larger amplitudes of vibration are more likely to trigger slip and shear modulus weakening
- The reduction and recovery of shear modulus is an important mechanism for triggering failure of earthquake-triggered landslides

Supporting Information:

Supporting Information may be found in the online version of this article.

Correspondence to:

W. Hu and H. Luo,
huwei1999@126.com;
1162639264@qq.com

Citation:

Hu, W., Luo, H., Xu, Q., McSaveney, M., Huang, R., Zheng, J., et al. (2022). Effect of amplitude and duration of cyclic loading on frictional sliding instability in granular media: Implication to earthquake triggering of landslides. *Journal of Geophysical Research: Solid Earth*, 127, e2022JB024488. <https://doi.org/10.1029/2022JB024488>

Received 30 MAR 2022
Accepted 30 OCT 2022

Author Contributions:

Conceptualization: Wei Hu, Hui Luo, Mauri McSaveney, Runqiu Huang, Jie Zheng, Yujie Wang

Data curation: Wei Hu, Hui Luo, Qiang Xu, Mauri McSaveney, Jie Zheng, Xiaoping Jia

Investigation: Jie Zheng

Resources: Hui Luo, Qiang Xu, Mauri McSaveney, Jie Zheng

Validation: Wei Hu, Hui Luo, Qiang Xu, Yujie Wang

Writing – original draft: Wei Hu, Hui Luo, Qiang Xu

Writing – review & editing: Wei Hu, Hui Luo, Qiang Xu

© 2022. American Geophysical Union.
All Rights Reserved.

Effect of Amplitude and Duration of Cyclic Loading on Frictional Sliding Instability in Granular Media: Implication to Earthquake Triggering of Landslides

Wei Hu¹ , Hui Luo¹, Qiang Xu¹, Mauri McSaveney^{1,2} , Runqiu Huang¹, Jie Zheng³, Yujie Wang³, and Xiaoping Jia⁴

¹State Key Laboratory of Geo-Hazard Prevention and Geo-Environment Protection, Chengdu University of Technology, Chengdu, China, ²GNS Science, Lower Hutt, New Zealand, ³School of Physics and Astronomy, Shanghai Jiao Tong University, Shanghai, China, ⁴Institut Langevin, ESPCI Paris, Université PSL, CNRS, Paris, France

Abstract Strong earthquakes with larger magnitude and longer durations trigger many landslides, however, how magnitude and duration affect landslides is still unclear. Many factors could contribute to this, including additional shear stress provided by strong ground motion, or “seismogenic liquefaction”; herein, we hypothesize that the dynamic weakening of sliding zone gouge is important. We explored the influence of earthquake magnitude and duration on landslide triggering by simulating the seismic response of sliding zone gouge using a dynamic ring-shear device and glass spheres. The experiments showed that vibration with larger amplitudes and longer durations more easily trigger deformation and even instability in dry granular materials. We used a dynamic triaxial-bender system to find that the shear modulus of these materials decreased with the increase in duration and amplitude of cyclic loading. We suggest that this universal decrease in shear modulus is an important landslide-trigger mechanism. Our results revealed how magnitude and duration of earthquakes affect co-seismic landslides and why earthquakes with larger magnitude and long durations can trigger more co-seismic landslides.

Plain Language Summary Strong earthquakes with larger magnitudes and longer durations trigger many landslides. Some mechanisms have been proposed to explain the triggering, for example, seismic waves provide additional driving force which increases the shear stress on the sliding plane. Earthquakes may cause an increase of pore pressure, which reduces the effective normal stress on the sliding plane. However, the mechanisms that apply to wet and dry conditions are not fully understood. We hypothesize that the dynamic weakening of sliding zone gouge caused by earthquakes is an important mechanism. We used a dynamic ring shear device and glass spheres to simulate the seismic response of sliding zone gouge, and our experiments show that larger amplitudes and longer durations more easily trigger deformation and even instability. Using a dynamic triaxial-bender system, we found that the shear modulus decreased with the increase in duration and amplitude of vibration. Our results reveal how earthquakes with larger magnitudes and long durations trigger more co-seismic landslides. Our experimental method may be helpful for monitoring and early warning of earthquake-triggered landslides in the future.

1. Introduction

Strong earthquakes are known to trigger large numbers of landslides in susceptible terrain (Chigira et al., 2010; Huang & Fan, 2013; Keefer, 1984, 2002; Massey et al., 2020). For instance, the 1999 Chi-chi Mw 7.6 earthquake in Taiwan caused 26,000 co-seismic landslides (Wang et al., 2002), the 2008 Wenchuan Mw 8.0 earthquake in China triggered more than 60,000 landslides (Huang & Fan, 2013), and the 2016 Kaikoura Mw 7.8 earthquake in New Zealand triggered 29,519 landslides (Massey et al., 2020). Studies of the seismic response of slope materials and the triggering mechanisms of slope instability are needed to improve the prediction of earthquake-triggered landslides (Indraratna et al., 2013).

The magnitude, duration, and frequency of seismic waves are important in earthquakes (Papazachos et al., 1982), and the distribution of earthquake-triggered landslides has been shown to correlate with these factors (Delgado et al., 2011; Jibson & Tanyaş, 2020; Keefer, 1984; Malamud et al., 2004; Martha et al., 2016). Based on a large dataset of earthquake-triggered landslide inventories, the maximum distribution area of triggered landslides is positively correlated with earthquake magnitude (Delgado et al., 2011; Keefer, 1984; Malamud et al., 2004), strong

ground acceleration (Martha et al., 2016) and duration, and negatively correlated with the frequency of the seismic waves (Jibson & Tanyaş, 2020). In general, the database shows that the distribution of earthquake-triggered landslides has regularities related to the amplitude, frequency and duration of seismic waves. However, research on the absolute impact of individual factors is still limited. Laboratory experiments can be used to isolate the influence of individual factors. Through sliding-block vibration experiments, Wang (1977) systematically summarized the influence of vibration factors, finding that large vibration amplitude, lower frequency and longer duration are more likely to trigger sliding. More controlled vibration shear experiments with granular materials are needed to further study the characteristics of seismic response and confirm the results of these initial studies.

Some mechanisms have been proposed to explain landslide triggering by earthquakes. Ground-motion acceleration provides additional shear stress (SS), and can cause the SS on the sliding surface to exceed the shear resistance (Dai et al., 2011; Lacroix et al., 2014; Meunier et al., 2007, 2008; Newmark, 1965; Wang & Zhang, 1982). Seismic loading can cause “seismogenic liquefaction” of the saturated layer above the sliding surface, leading to a drop in effective normal stress, and thus causing a decline in shear resistance on the sliding surface (Cui et al., 2016; Sassa et al., 2004, 2007; Wang et al., 2013; Wang, Huang, et al., 2014; Wang, Suemine, et al., 2014; Xu et al., 2012). Multiple ground motion cycles crush soil grains and fracture rock masses on the shearing plane, decreasing the shear resistance of the sliding surface (Bontemps et al., 2020; Meunier et al., 2008). This mechanism can explain the amplitude and duration effects of earthquake-triggered landslides in dry or wet conditions, but field validation and quantitative analysis are lacking.

We propose that dynamic weakening of the shear modulus of the sliding zone gouge has a function in landslide triggering because many researchers observe a temporary decrease in shear modulus or shear-wave velocity under vibration in the laboratory and field (Bontemps et al., 2020; Jia et al., 2011; Johnson et al., 2008, 2012, 2016; Johnson & Jia, 2005; Léopoldès et al., 2020; Zhou & Chen, 2005). But experimental and field evidence on how earthquakes with different amplitudes and durations affect shear modulus and how shear modulus changes affect slip and instability are still lacking.

Therefore, we conducted ring-shear cyclic loading tests with different amplitudes and durations using 0.2–0.4 mm glass spheres (SiO_2) in a dry condition. At the same time, we recorded acoustic emission (AE) signals using an AE acquisition system. Moreover, we measured changes in shear modulus of the same material using a dynamic triaxial bender system. Our study highlighted the influence of vibration duration and amplitude on triggering and the effect of shear modulus changes.

2. Apparatus and Methods

We used a ring shear apparatus to study the mechanical behavior of samples of dry glass spheres (SiO_2) under cyclic loading and used triaxial tests to monitor the evolution of the shear modulus of samples under cyclic loading.

In nature, co-seismic landslides may be affected by many types and different directions of seismic waves. These seismic waves, acting on the sliding zone, can be resolved into components of seismic acceleration vertical and parallel to the sliding surface (Figure 1a). The ring shear instrument can apply dynamic loading of different amplitudes and durations to granular materials while providing constant normal stresses and SSs, simulating the natural stress state of sliding zone gouge under seismic waves (Figure 1b). Glass spheres are widely used in laboratory experiments to study the geophysical mechanisms of fault (Jia et al., 2011; Johnson et al., 2008, 2012, 2016; Johnson & Jia, 2005; Léopoldès et al., 2020). In our experiments, the granular medium was composed of glass spheres (SiO_2) with a diameter of 0.2–0.4 mm.

2.1. Dynamic Ring Shear Apparatus

We used ring shear cyclic loading testing to study the dynamic response of dry granular materials. The setup of the ring shear apparatus is shown in Figure 1c. In the experiments, firstly, 0.2–0.4 mm glass spheres (SiO_2) were placed in a ring shear box ($H = 66.2$ mm, $D_s = 21$ mm) with an initial density of 1.52 g/cm^3 (initial total porosity of 37.7%), and constant normal stress and constant SS were then applied. Then, under these stress states, sinusoidal cyclic SS or cyclic normal stress with different numbers of cycles and amplitudes were applied respectively. In the experiments, the frequency of cyclic loading was 1 Hz (1 cycle/s), which can represent the typical dominant

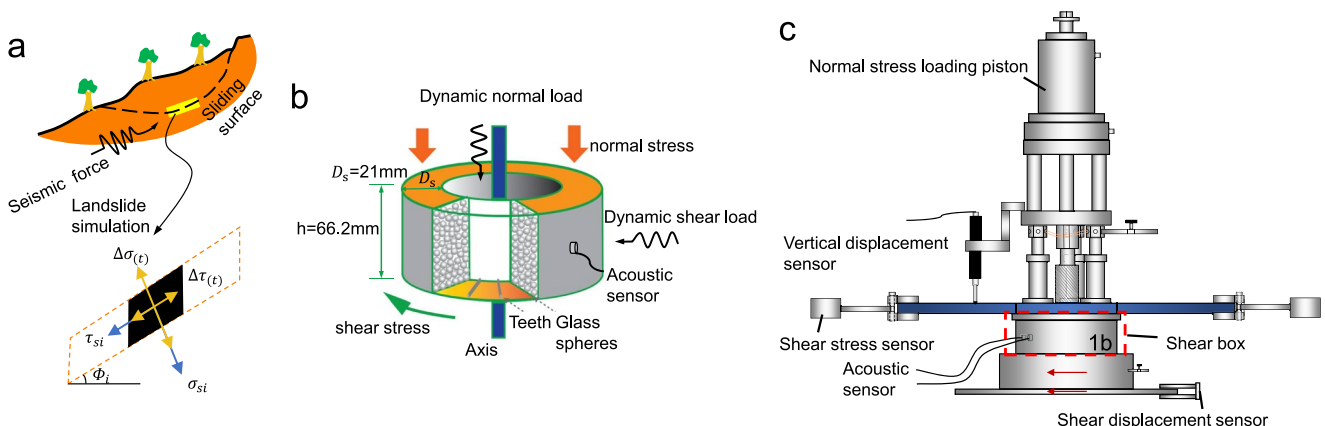


Figure 1. The model of co-seismic landslide and ICL-2 ring shear apparatus. (a) Model of landslide sliding zone and mechanical model of unit cell under seismic force. (b) Physical model of ring shear experiment. (c) Schematic of ICL-2 ring shear test system. Section modified from Cui et al. (2016). σ_{si} - static normal stress, τ_{si} - static shear stress, $\Delta\tau_{(t)}$ - dynamic shear stress, $\Delta\sigma_{(t)}$ - dynamic normal stress.

frequencies of the earthquake ground motions (Trifunac, 2008; Wang et al., 2013). Test conditions are shown in Table 1. Further details of the ring shear apparatus are given in Supporting Information S1.

2.2. Acoustic Emission Acquisition System

During these ring shear experiments, continuous acquisition, collected by an NI (National Instrument Company, USA) compact DQA, PXle-1084 & BNC-2110 acoustic emission sensor (WD), was installed near the shear zone to record the elastic waves generated in the experiments (Figure 1b). AE signals were amplified by 40 dB and digitized with a sampling rate of 1 MHz. The sampling rate of 1 MHz is much higher than the 1 Hz vibration frequency and can distinguish data in the 0–500,000 Hz frequency range. The time-frequency diagrams were obtained from the short-time Fourier transform of the AE signals. The setup of AE acquisition system is shown in Figure S1 in Supporting Information S1.

2.3. Dynamic Triaxial-Bender Systems

To study the evolution of the shear modulus of the sample during cyclic loading, we conducted a set of dynamic triaxial bender experiments. In the experiment, 0.2–0.4 mm glass spheres were used to make a specimen with a height of 200 mm, a diameter of 100 mm, and an initial density of 1.569 g/cm³ (initial total porosity of 35.7%). The specimen was put into a triaxial cell, and a confining pressure of 300 kPa and deviatoric stress of 380 kPa were applied. Sinusoidal cyclic dynamic loads with amplitudes of 15 kPa, 45 kPa, and 75 kPa, a frequency of 1 Hz (1 cycle/s) and a cycle number of 200 were applied. The frequency was the same as that in the ring shear test. During the dynamic loading, we used a bender element system to obtain the corresponding change in the shear modulus of the specimen with an interval time of 273 ms. In the ring shear and dynamic triaxial experiments, the glass spheres were under dry conditions (room humidity) and remained unbroken in the samples. The setup of the dynamic triaxial bender system is shown in Figure 2. Further details on this system are given in Supporting Information S1.

The bender element system obtains the small-strain shear modulus (G_{max}) of the sample by measuring the shear wave propagation velocity (Shirley & Hampton, 1978), while the small-strain shear modulus is close to the maximum shear modulus, as the bender element test causes minimal disturbance to the specimen. The calculation method is as follows:

$$V_s = H / (T_a - T_0)$$

$$G_{max} = \rho V_s^2$$

where V_s = shear wave velocity, H = propagation distance (the distance from tip to tip between bender elements), T_a = arrival time, T_0 = initial time, G_{max} = small-strain shear modulus, and ρ = bulk density of soil.

Table 1
Test Schemes of Dynamic Ring Shear Tests

Constant normal load (kPa)	Peak shear stress (kPa)	Constant shear stress (kPa)	Ratio of SS to PSS	Amplitude			Number of cycles	Test number
				Dynamic normal load	Dynamic shear load			
300	191	173	0.906	0	30		5	Test-1
							10	Test-2
							20	Test-3
300	189	172	0.91	20	0		5	Test-4
							20	Test-5
							40	Test-6
100	70	63	0.9	0	29		5	Test-7
							20	Test-8
							40	Test-9
100	75	68	0.907	30	0		5	Test-10
							20	Test-11
							40	Test-12
500	320	292	0.913	0	40		5	Test-13
							10	Test-14
							20	Test-15
500	320	292	0.913	20	0		5	Test-16
							10	Test-17
							20	Test-18
300	207	187	0.9	0	20		10	Test-19
							30	Test-20
							40	Test-21
300	204	186	0.91	20	0		10	Test-22
							40	Test-23
							50	Test-24

Note. SS = constant shear stress; PSS = peak shear stress.

Several methods of determining the propagation time of S-wave velocity have been proposed, such as a first break, peak-to-peak, cross-correlation, or a phase/frequency relationship (Clayton, 2011). In this study, the peak-to-peak method was used to determine the travel time of the S-wave, and the distance between the peak value of the transmitted wave and the first peak of the received wave was regarded as the propagation time (Figure 3).

3. Results

3.1. Dynamic Ring Shear Experiments With Different Numbers of Cycles (Duration of Vibration)

Figure 4 shows the ring shear experimental results under different numbers of cycles of sinusoidal dynamic shear loads with an amplitude of 30 kPa and frequency of 1 Hz under 300 kPa normal stress and 173 kPa SS (Test 1 to Test 3). The peak shear strength of the sample was 191 kPa (PSS), and the ratio of SS to PSS was 0.906.

The results show that shear displacement showed three different forms with differing numbers of cycles (Figures 4b, 4f and 4j). We defined the co-vibration slip and the post-vibration slip—the shear displacement of the sample during and after the vibration. For five cycles, the shear displacement only had a small co-vibration slip (0.16 mm), and the displacement stopped immediately as soon as the vibration ended (Figure 4b). For 10 cycles, larger co-vibration slip occurred (0.854 mm), and a period of decelerating shear displacement (0.534 mm), known as the “relaxation period” (Bontemps et al., 2020), followed at the end of the vibration (Figure 4f). When the

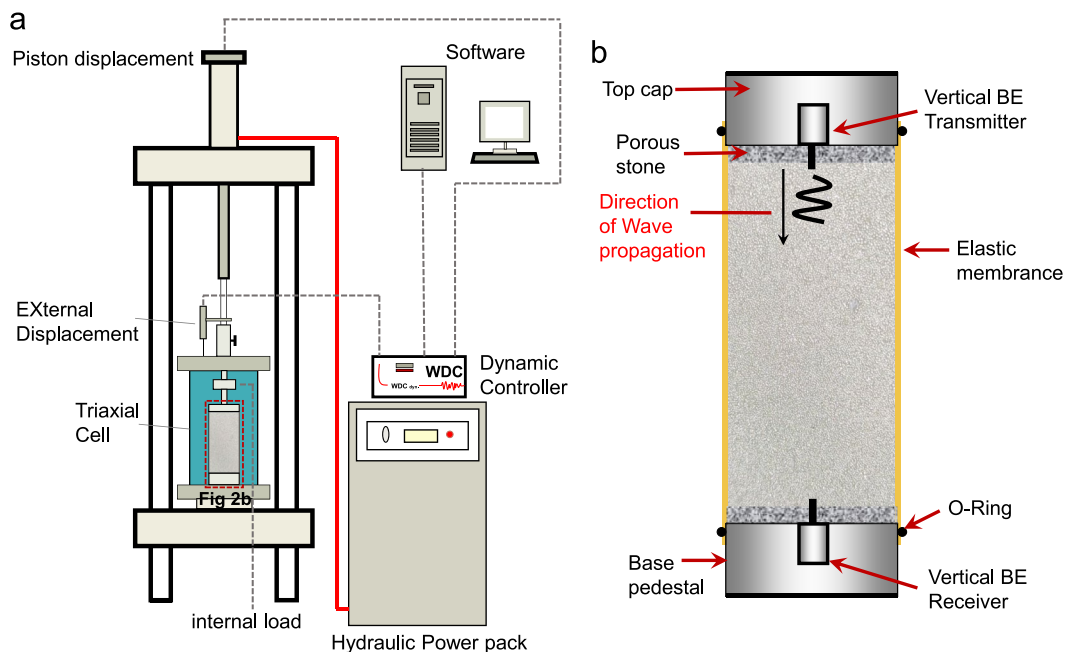


Figure 2. Dynamic triaxial test system with bender element. (a) Schematic of dynamic triaxial test system. (b) Bender elements on a triaxial sample.

number of cycles was 20, the shear displacement underwent 2.25 mm of co-vibration slip, and was followed by an accelerated motion that did not stop spontaneously after the vibration ended, showing the instability (Figure 4j). The co-vibration and post-vibration shear displacements thus increased with an increase in the number of cycles, and the instability of granular materials can be triggered by a larger number of cycles.

It was also observed that vibrating the SS caused a stepwise increase of co-vibration shear displacement, but caused little change in normal stress and vertical displacement (Figures 4b, 4f and 4j). We enlarged the curves of shear displacement in Figures 4f and 4j (see Figure 5a and Figure 5c), respectively. The stepwise increase curves of co-vibration shear displacement show platform segments and upward segments (Figures 4f and Figures 5a, 5c);

the platform segments corresponded to trough segments of cyclic SS, and the upward segments to crest segments of cyclic SS (Figure 4f). It shows that the deformation was promoted by the increase of SS. Meanwhile, the curves also show that the shear displacement value of each upward segment was not the same, but increased with the increase in the number of vibration cycles, following a logarithmic law (Figures 5b and 5d). This means that the rate and acceleration of each upward segment increased with the increase in the number of vibration cycles. When the vibration ended, the co-vibration shear displacement remained stable in the form of the platform (Figures 5a and 5c), and the SS of the three experiments returned to an initially constant value.

Figures 4c, 4g and 4k shows the amplitude of AE energy released during experiments, and Figures 4d, 4h, and 4l shows the frequency and energy intensity of the AE signal derived from the Fourier transform of Figures 4c, 4g, and 4k. AE results can reflect the state and velocity of motion. Before the vibration started, the sample was in a static state, and there is no AE signal. In the vibration process, the stepwise increase of co-vibration shear displacement was also shown by periodic changes of AE signal and energy in the AE signal diagrams (Figures 4c, 4g and 4k) and time-frequency diagrams (Figures 4d, 4h and 4l). As shown in Figures 4c, 4g, and 4k, the AE signals of upward segments of co-vibration shear displacement have a larger amplitude than the platform segments have. Figures 4d, 4h, and 4l also show

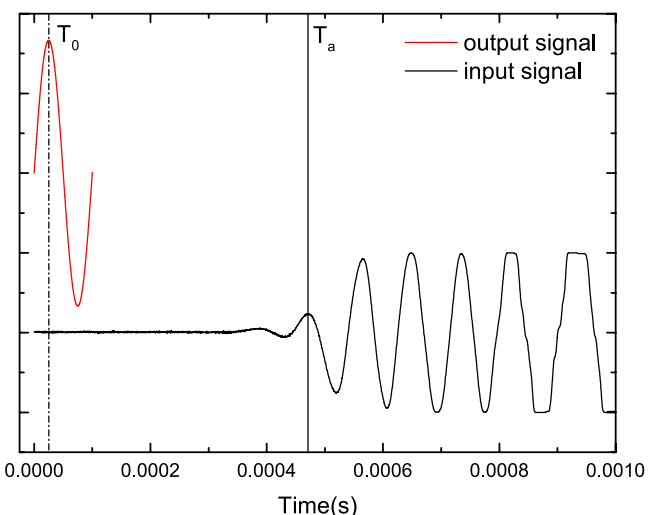


Figure 3. Typical record of transmitter and receiver signals of bender elements and identification of shear-wave traveling time feature points. T_0 -initial time, T_a -arrival time.

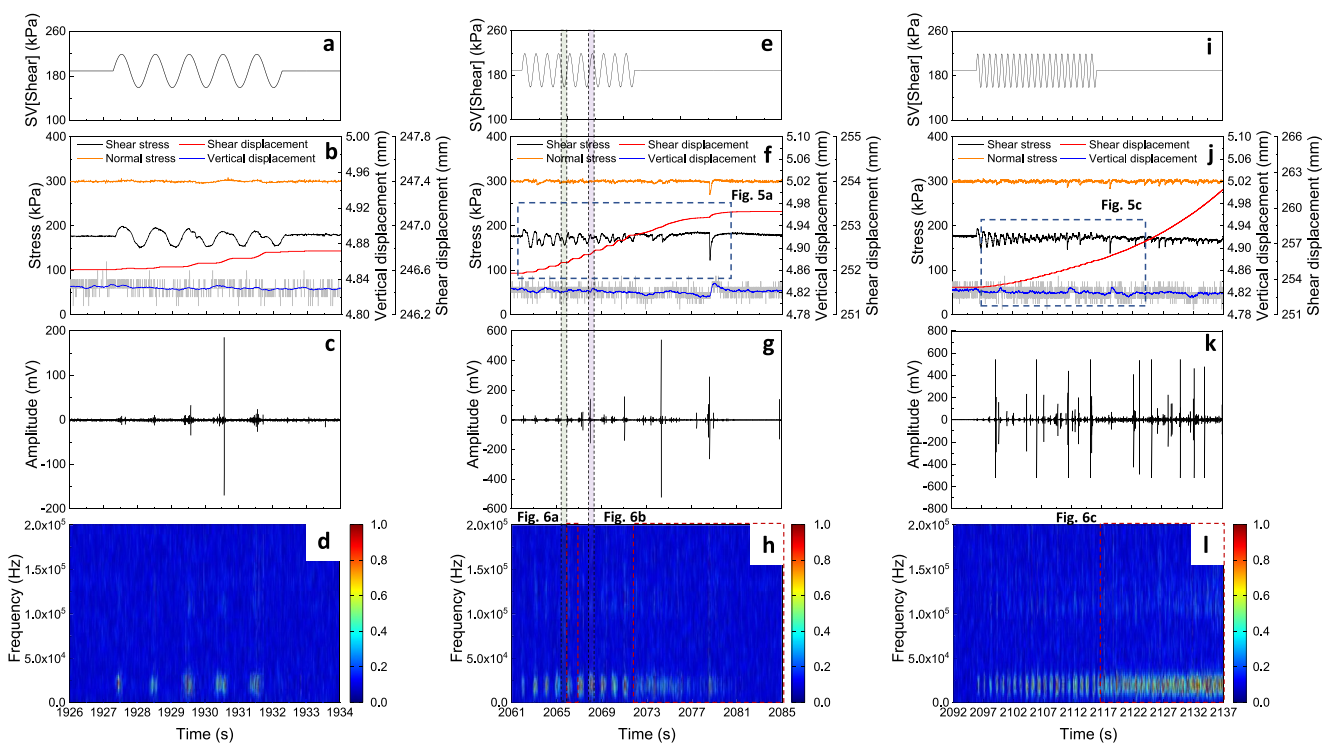


Figure 4. Cyclic shear loading tests at different numbers of cycles under 300 kPa normal stress and 173 kPa shear stress (Test 1 to Test 3). (a), (e), (i) are the graphs of the input sinusoidal dynamic load, the amplitude is 30 kPa, the frequency is 1 Hz, the number of cycles is 5, 10, and 20, respectively. (b), (f), (j) are the graphs of experimental results, showing the change of normal stress (orange line), shear stress (black line), shear displacement (red line), and vertical displacement (blue line). (c), (g), (k) are diagrams of acoustic emission original signals during the experiment. (d), (h), (l) are acoustic emission time-frequency diagrams during the experiment. In (e), (f), (g) and h, the green rectangle shows the platform segment of co-vibration shear displacement, and the purple rectangle shows the upward segment.

that the frequencies of upward segments have a much larger energy intensity than the platform segments in the frequency range of 0–50 kHz, and also have a larger energy intensity in the range of 90–150 kHz (Figure 6a). Figures 6b and 6c shows that the time-frequency of post-vibration motion is completely different from that of the vibration process. For the post-vibration motion that decelerated and eventually stopped, the corresponding AE signals also gradually weakened and disappeared, while there was no high frequency signal (Figure 6b). For the

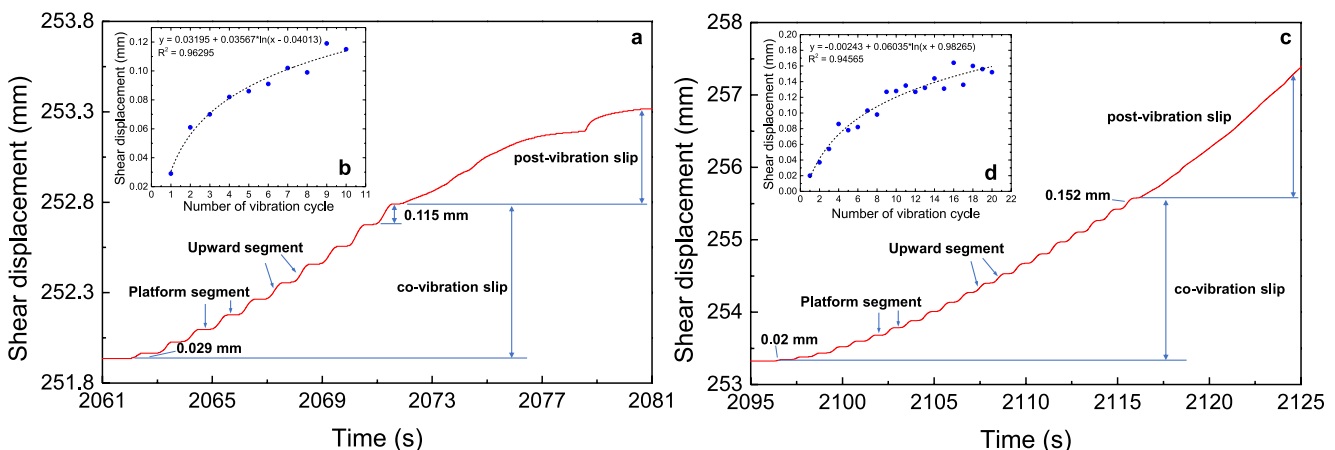


Figure 5. The changes of shear displacement. (a) and (c) are the changes of shear displacement including co-vibration slip and post-vibration slip, and show the stepwise increase of co-vibration slip, enlarged from Figures 4f and 4j. (b) and (d) show that the shear displacement of each upward segment increased with the increase in the number of vibration cycles.

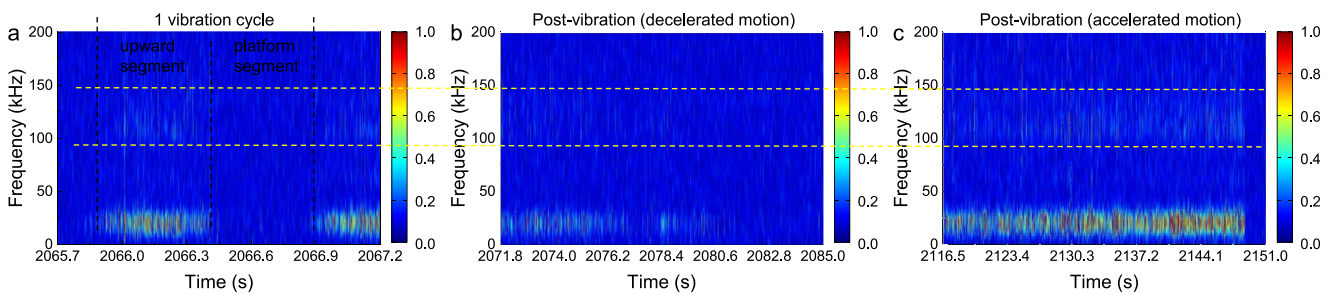


Figure 6. Acoustic emission time-frequency diagrams. (a) The time-frequency diagram during vibration, enlarged from Figure 4h. Black dashed line shows the upward segment and platform segment in a cycle of vibration. (b) The time-frequency diagram after vibration, enlarged from Figure 4h. (b) The time-frequency diagram after vibration, enlarged from Figure 4i. Yellow dashed line shows the frequency range of the high-frequency signal.

post-vibration motion that accelerated, the corresponding AE signals gradually became stronger, and had a high frequency signal that gradually increased with time (Figure 6c).

It was observed that low-frequency (few tens of kHz) AEs are generated during grain friction, while grain collision and crushing excites high-frequency (hundreds of kHz) AEs (Lin et al., 2019; Mao et al., 2018; Michlmayr & Cohen, 2014). While no grain breakage was observed after our tests, in fact, during the co-vibration slip, the acoustic signals with low frequency were mostly from the friction of particles. For the post-vibration slip of decelerated motion (Figure 6a), the acoustic signals with low frequency were also from inter-particle friction (Figure 6b). However, for the post-vibration slip with accelerated motion, the acoustic signals with high frequency were from the collision of the particles during rapid shearing (Figure 6c).

We counted the energy amplitudes corresponding to the frequencies in each upward segment of three sets of cyclic shear loading tests with different numbers of cycles (Figure 7). The results show that the intensity of acoustic frequency of upward segments increased with the increase in the number of vibration cycles in the frequency range of 0–50 kHz (Figures 7b, 7d, and 7f), and the high frequency (90–150 kHz) signal gradually becomes stronger (Figures 7a, 7c, and 7e).

We next applied dynamic normal loads of different numbers of cycles with an amplitude of 20 kPa and a frequency of 1 Hz under 300 kPa normal stress, and 172 kPa SS (Test 4 to Test 6). The peak shear strength of the sample was 189 kPa (PSS), and the ratio of SS to PSS was 0.91.

We obtained the same result: a larger number of cycles of dynamic normal load produced a larger co-vibration shear displacement and post-vibration shear displacement and could trigger instability. The difference was that vibrating normal stress caused fluctuations of the SS and vertical displacement synergistically (Figures 8b, 8f, and 8j). The shear displacement also showed a stepwise increase; however, in the dynamic normal load experiments, the upward segments of shear displacement corresponded to the trough segments of cyclic normal stress (Figures 8b, 8f, and 8j), which was the opposite to the results of the dynamic shear loads experiments (Figures 4b, 4f, and 4j). This shows the different dynamic response mechanisms of effective normal stress reduction and particle dilation. In the dynamic normal load experiments, as the number of vibration cycles increased, the platform

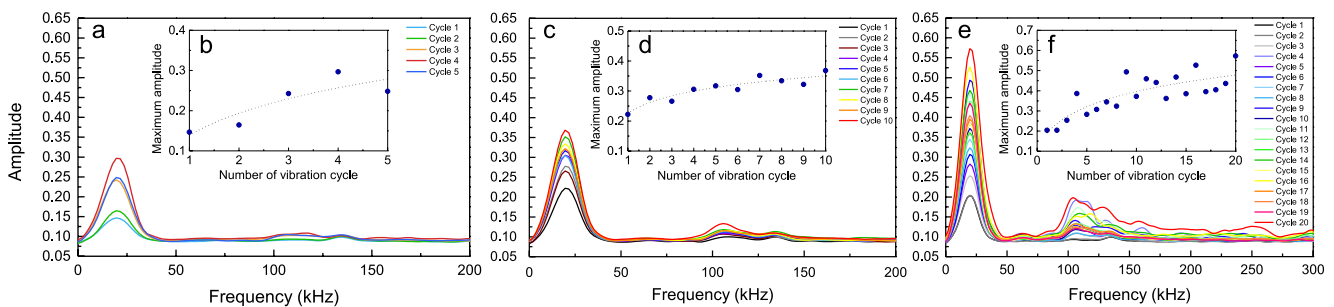


Figure 7. Variation of AE frequency and energy amplitude of upward segments with the number of vibration cycles (Test 1 to Test 3). (a), (c), (e) are the graphs of AE energy and frequency changes in the upward segments of each vibration cycle in tests 1–3. (b), (d), and (f) are the graphs of the variations of the frequency energy peaks corresponding to each upward segment, in the frequency range 0–50 kHz.

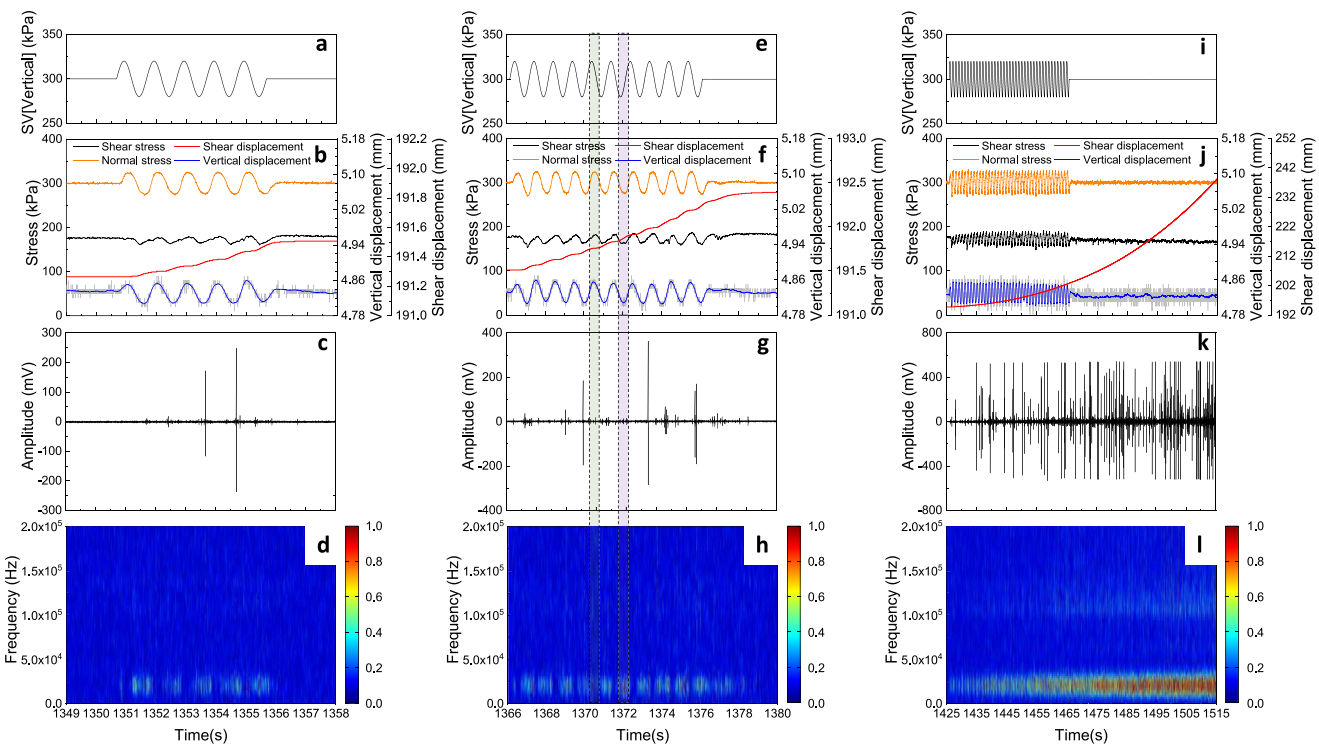


Figure 8. Cyclic normal loading tests at different numbers of cycles under 300 kPa normal stress and 172 kPa shear stress (Test 4 to Test 6). (a), (e), (i) are the graphs of the input sinusoidal dynamic load, the amplitude is 20 kPa, the frequency is 1 Hz, the number of cycles is 5,10, and 40, respectively. (b), (f), (j) are the graphs of experimental results, showing the change in normal stress (orange line), shear stress (black line), shear displacement (red line), and vertical displacement (blue line). (c), (g), and (k) are diagrams of acoustic emission original signals during the experiment. (d), (h), and (l) are acoustic emission time-frequency diagrams during the experiment. In e, f, g, and h, the green rectangle shows the platform segment of shear displacement, and the purple rectangle shows the upward segment.

segments gradually transformed into upward segments which have a smaller slope than upward segments have (Figures 8f and 8j).

Similar experimental results were obtained under 100 kPa (Figures S2 and S3, Test 7 to Test 12 in Supporting Information S1) and 500 kPa (Figures S4 and S5, Test 13 to Test 18 in Supporting Information S1) normal stresses. A larger number of vibration cycles can cause larger co-vibration and post-vibration shear displacement, and are more likely to trigger instability in the samples.

Figure 9 presents the changes in shear displacement of each upward segment from test 1 to test 18. It shows that the shear displacement of each upward segment increased with an increase in the number of vibration cycles in both dynamic shear load and dynamic normal load experiments under 100 kPa, 300 kPa, and 500 kPa normal stress (Figure 9). Figure 10 shows that the post-vibration shear displacement also increased with the increase in the number of vibration cycles, and instability occurred eventually. These results indicate that the shear strength of granular materials may show a duration-dependent dynamic weakening under different normal stresses of 100 kPa, 300 kPa, and 500 kPa. The increase of shear displacement of each upward segment roughly followed a logarithmic law in the dynamic shear loads experiments (Figures 9a, 9c and 9e), and linearity in the dynamic normal loads experiments (Figures 9b, 9d and 9f).

3.2. Dynamic Ring Shear Experiments With Different Amplitudes

We also studied the influence of amplitude on dynamic triggered sliding. Figure 11 shows the results under different amplitudes of sinusoidal dynamic shear loads with 10 cycles and a frequency of 1 Hz under 300 kPa normal stress and 187 kPa SS (Test 19 to Test 21). The peak shear strength of the sample was 207 kPa (PSS), and the ratio of SS to PSS was 0.9. The results show that the vibration with an amplitude of 40 kPa triggered instability (Figure 11j), while vibrations with amplitudes of 20 and 30 kPa only caused small co-vibration slip of 0.34 and 1.093 mm respectively (Figures 11b and 11f).

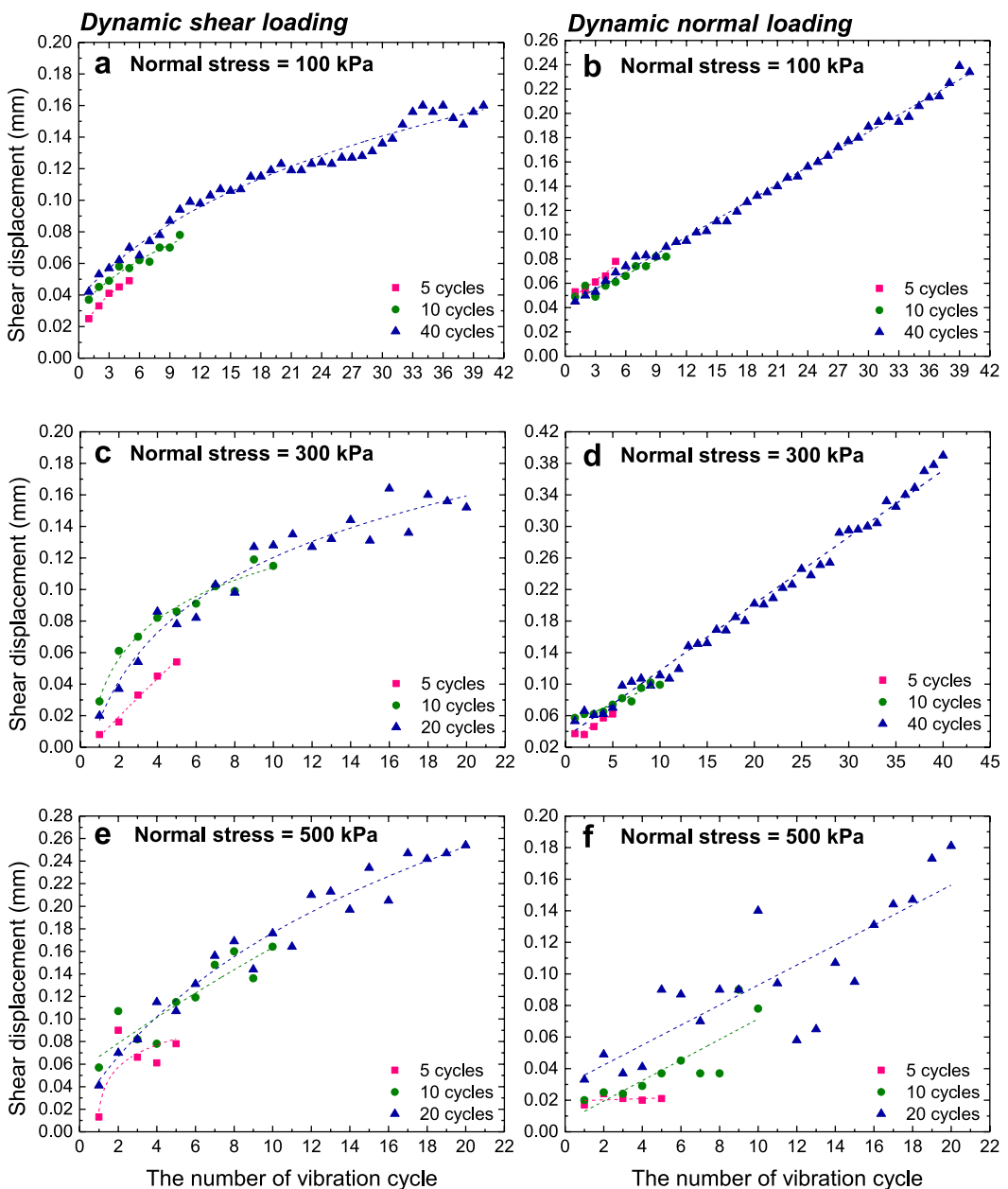


Figure 9. The changes of shear displacement of each upward segment with increases in the number of vibration cycles in dynamic shear load experiments and dynamic normal load experiments under 100 kPa, 300 kPa, and 500 kPa normal stress. (a), (b) The shear displacement of each upward segment increased with the increase in the number of vibration cycles in both dynamic shear load experiments (a) and dynamic normal load experiments (b). (c), (d) The shear displacement of each upward segment increased with the increase in the number of vibration cycles in both the dynamic shear load experiments (c) and dynamic normal load experiments (d). (e), (f) The shear displacement of each upward segment increased with the increase in the number of vibration cycles in both the dynamic shear load experiments (e) and dynamic normal load experiments (f).

Similar results were obtained in the dynamic normal loading tests. Figure 12 shows the results for different amplitudes of sinusoidal dynamic normal loads with 10 cycles and a frequency of 1 Hz under 300 kPa normal stress and 186 kPa SS (Test 22 to Test 24). The peak shear strength of the sample was 204 kPa (PSS), and the ratio of SS to PSS was 0.91. When the amplitude was 20 kPa, the vibration caused only a small co-vibration slip (0.652 mm) (Figure 12b). When the amplitude was 40 kPa, the shear displacement underwent 2.004 mm co-vibration slip

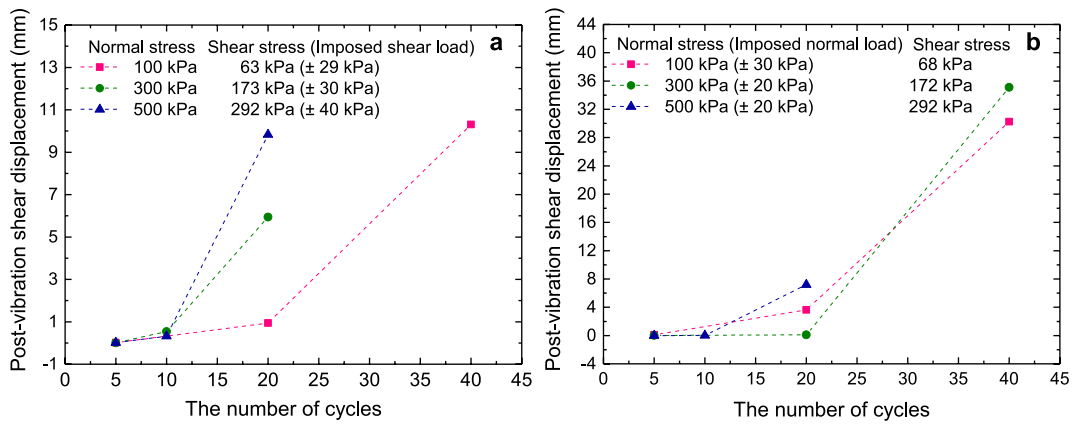


Figure 10. The changes in post-vibration shear displacement with an increase in the number of vibration cycles in dynamic shear load experiments and dynamic normal load experiments under 100 kPa, 300 kPa, and 500 kPa normal stress. (a) The post-vibration shear displacement increased with the increase in the number of vibration cycles in the dynamic shear load experiments (a), and in the dynamic normal load experiments (b).

and a period of decelerating post-vibration slip (5.678 mm) (Figure 12f). When the amplitude was 50 kPa, the vibration caused instability (Figure 12j).

Figure 13 presents the changes in shear displacement of each upward segment from Test 19 to Test 24. The results show that the shear displacement of each upward segment increased with the increase in the number of vibration cycles, and it shows that the larger the amplitude, the larger the shear displacement of the upward segment in the

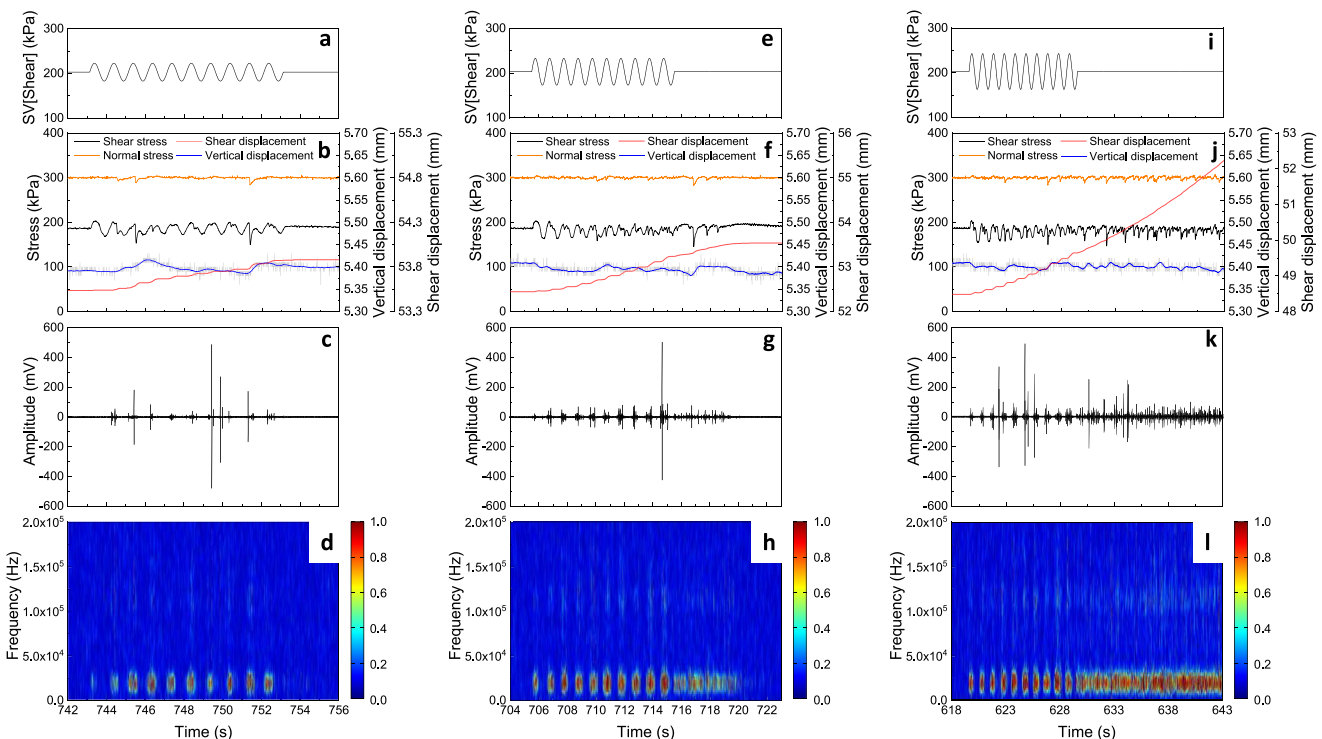


Figure 11. Cyclic shear loading tests at different amplitudes under 300 kPa normal stress and 187 kPa shear stress (Test 19 to Test 21). (a), (e), and (i) are the graphs of the input sinusoidal dynamic load, the number of cycles is 10, the frequency is 1 Hz, and the amplitudes are 20 kPa, 30 kPa, and 40 kPa, respectively. (b), (f), and (j) are the graphs of experimental results, showing the change of normal stress (orange line), shear stress (black line), shear displacement (red line), and vertical displacement (blue line). (c), (g), and (k) are diagrams of acoustic emission original signals during the experiment. (d), (h), and (l) are acoustic emission time-frequency diagrams during the experiment.

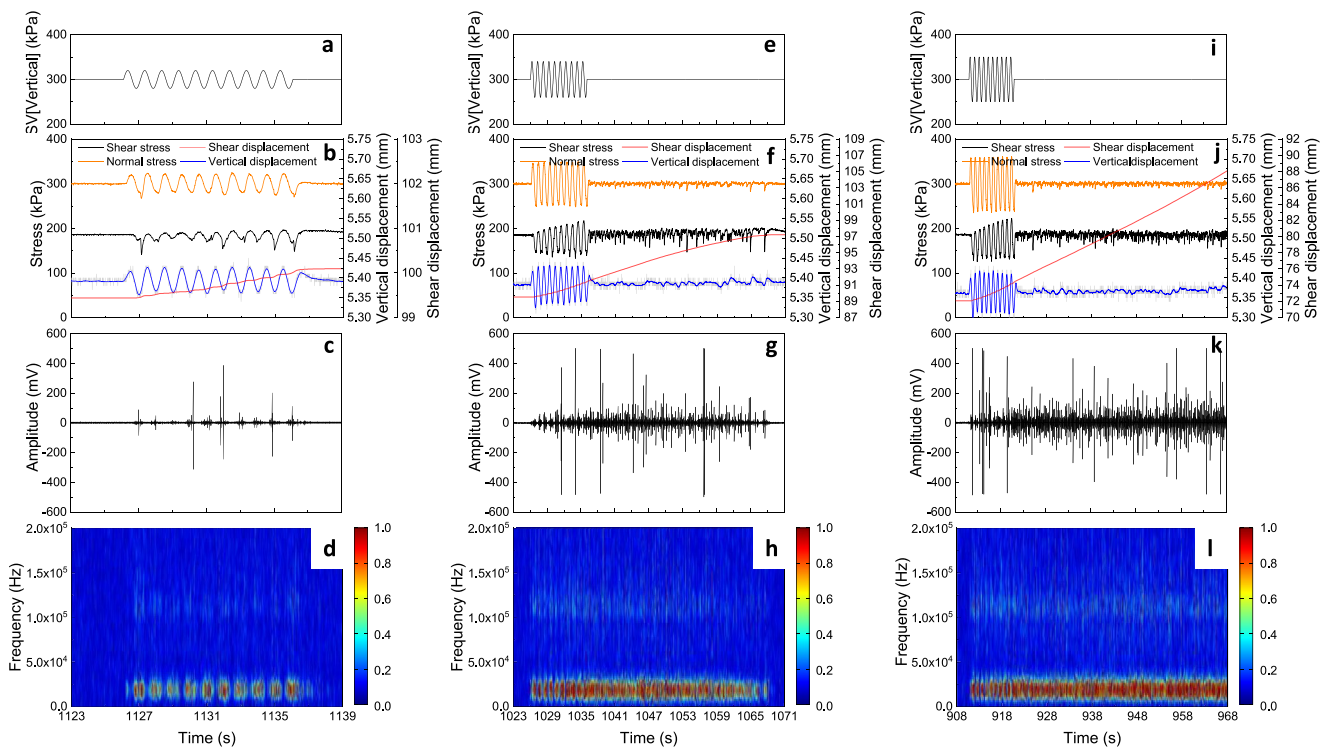


Figure 12. Cyclic normal loading tests at different amplitudes under 300 kPa normal stress and 186 kPa shear stress (Test 22 to Test 24). (a), (e), and (i) are the graphs of the input sinusoidal dynamic load, the number of cycles is 10, the frequency is 1 Hz, and the amplitude is 20 kPa, 40 kPa, and 50 kPa, respectively. (b), (f), and (j) are the graphs of experimental results, showing the change of normal stress (orange line), shear stress (black line), shear displacement (red line), and vertical displacement (blue line). (c), (g), and (k) are diagrams of acoustic emission original signals during the experiment. (d), (h), and (l) are acoustic emission time-frequency diagrams during the experiment.

same number of vibration cycles (Figures 13a and 13b). The post-vibration shear displacement increased with the increase in the amplitude (Figure 13c).

3.3. Dynamic Triaxial-Bender Tests

To further study the influences of vibration duration and amplitude on the dynamic weakening of samples, we conducted a set of dynamic triaxial bender experiments to observe the changes of shear modulus. The experiments were under 300 kPa cell pressure and 380 kPa deviatoric stress, with 200 cycles of sinusoidal dynamic loads with different amplitudes, and a frequency of 1 Hz.

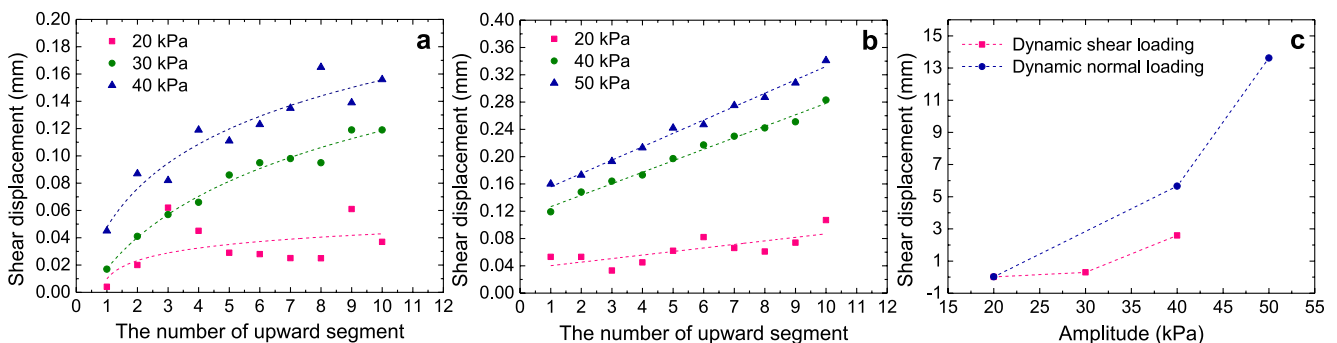


Figure 13. The changes of shear displacement of each upward segment and post-vibration shear displacement with the increase of amplitude in dynamic shear load experiments and dynamic normal load experiments under 300 kPa normal stress. (a) The shear displacement of each upward segment increased with the increase in the number of vibration cycles and amplitudes in both the dynamic shear load experiments (a), and in the dynamic normal load experiments (b). In (c) the post-vibration shear displacement increased with the increase in amplitudes.

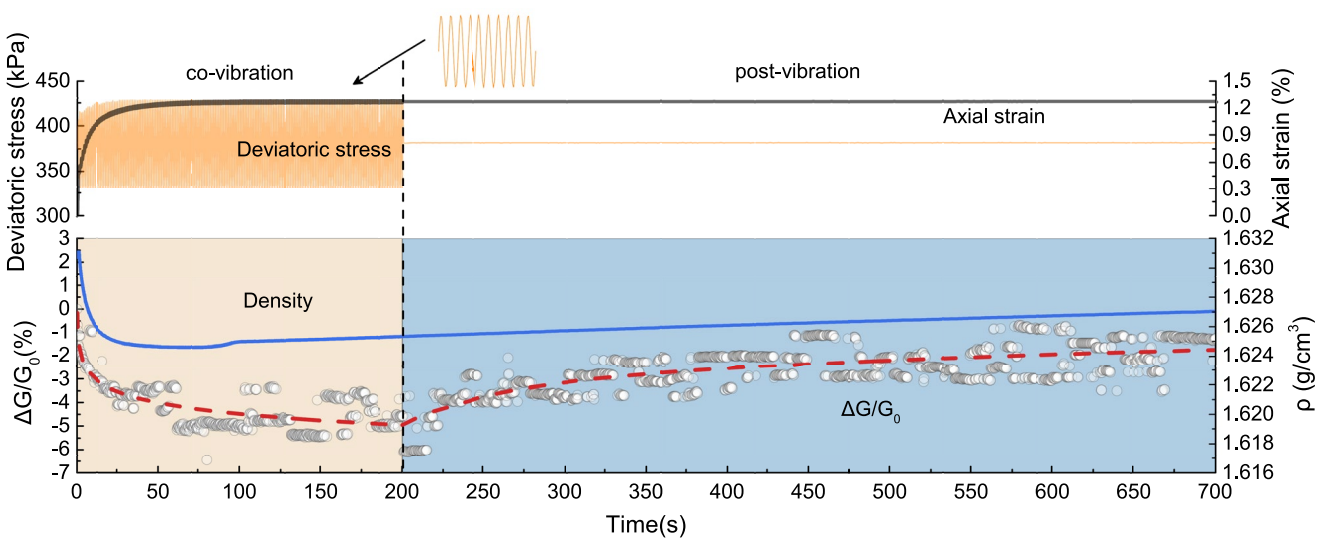


Figure 14. Dynamic triaxial bender test under 300 kPa cell pressure and a 380 kPa deviatoric stress. The amplitude of vibration is 45 kPa, the frequency is 1 Hz, and the number of cycles is 200. The graph shows the change of deviatoric stress (orange line), vertical strain (gray line), density (blue line), and shear modulus (red dash line and gray cycle) under cyclic loading.

The result shows that under the amplitude of 45 kPa, the specimen shear modulus decreased with the increase of the number of vibration cycles nonlinearly, with a maximum change of -6.45% , and reached a steady state after about 64 cycles during the vibration (Figure 14). The change of density has a similar tendency and decreased slightly by -0.374% . The axial strain increased nonlinearly and reached a steady state at a value of 1.26% . During vibration, the changes of shear modulus, density, and axial strain roughly follow a logarithmic law.

The changes of shear modulus include two forms of continuous gradual changes, and discontinuous abrupt changes also can be observed. The gradual changes show periodic variation corresponding to deviator stress and axial strain, and the shear modulus difference between two adjacent points is about 0.05% . The discontinuous abrupt changes of shear modulus show a larger change, and the maximum abrupt change in the shear modulus occurred at about 61 vibration cycles, when the shear modulus suddenly changed by -1.15% .

When the vibration ended, the shear modulus slowly recovered, following an approximate logarithmic law, known as an “aging effect” (Jia et al., 2011) or “stress relaxation” (Hartley & Behringer, 2003), while the density increased slightly. The experimental results with cyclic loading amplitudes of 15 kPa (Figure S6 in Supporting Information S1) and 75 kPa (Figure S7 in Supporting Information S1) give similar results. The differences are that the amplitude of 15 kPa caused smaller changes in the shear modulus (-3.5%), axial strain (0.276%), and density (-0.085%), compared with that of 45 kPa. The amplitude of 75 kPa caused larger changes in the shear modulus (-7.25%), axial strain (2.69%), and density (-0.725%) (Figure 15).

4. Discussion

4.1. Vibration Weakening of the Shear Modulus Triggers Slip and Instability

How does the weakening of the shear modulus affect landslide triggering? The shear modulus is an important parameter for predicting the shear deformation behavior of soils (Seed & Idriss, 1970). Johnson and Jia (2005) proposed that the reduction of shear modulus represents weakening of the material strength of the fault gouge, resulting in failure. Léopoldès et al. (2020) studied the ultrasound triggering of a granular avalanche on a slope, and proposed that the granular avalanche occurred because of the reduction of the coefficient of friction caused by ultrasound. Similar results have been observed in the field in that co-seismic slip occurred while the relative seismic velocity caused by an earthquake decreased in the landslide body (Bontemps et al., 2020). In our dynamic ring shear experiments, before the vibration, the sample was stable and there was no shear displacement, as the shear resistance of the sample was greater than the SS. After the vibration ended, while the SS returned to the initial value, post-vibration deformation and instability occurred (Figures 4j and 6j). This suggested that the shear

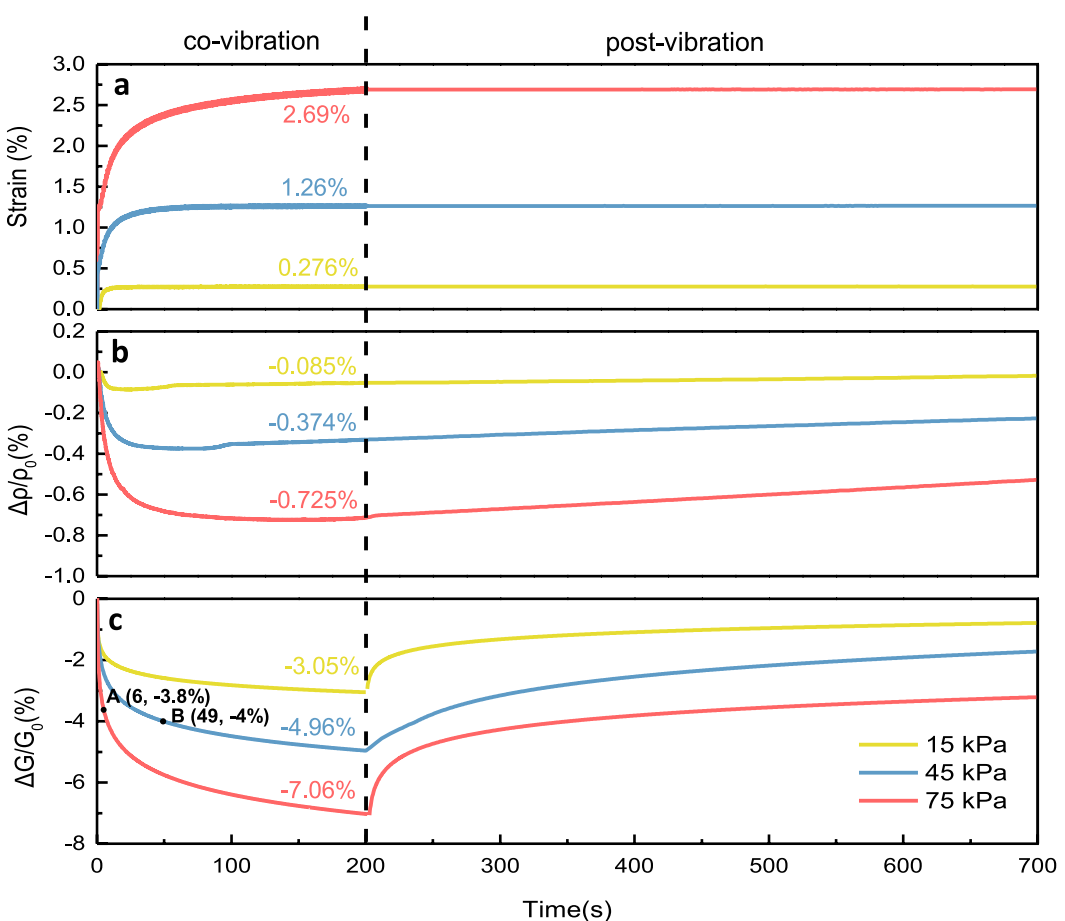


Figure 15. Comparison of strain, density and shear modulus changes with different vibration amplitudes. (a) The changes of strain with different vibration amplitudes. (b) The changes in density with different vibration amplitudes. (c) The changes of shear modulus with different vibration amplitudes.

resistance had decreased due to vibration and the decrease was dependent on the number of vibration cycles. The experiments using the dynamic triaxial-bender has similar results: the shear modulus was weakened by vibration and was dependent on the vibration duration that the shear modulus decreased by 3.5%, 6.45%, and 7.25% after 200 vibration cycles at 15 kPa, 45 kPa, and 75 kPa, respectively (Figure 15). When the shear resistance after vibration was greater than the SS, no post-vibration slip occurred in the sample, and when the shear resistance after vibration was smaller than the SS, the sample developed post-vibration slip or instability. Therefore, the mechanism of duration-dependent dynamic triggering can be understood: the larger the number of the vibration cycles there are, the smaller the shear modulus, and the lower the strength of the sample, the more likely it is to produce larger post-vibration shear displacement and instability.

In addition, the dynamic ring shear experimental results show that the shear displacement of each upward segment increased with the increase in the number of vibration cycles. The results of the AE signal show that the intensity of the frequency of upward segments increased with the increase in the number of vibration cycles (Figure 7), indicating the intensification of friction and collision between particles, which has the same trend as the change of shear displacement in the vibration process. This is consistent with the decrease of shear modulus during vibration. The decrease in shear modulus and increase in shear displacement of each upward segment in the dynamic shear load experiments have similar logarithmic trends (Figures 9a, 9c and 9e, Figure 14). In dynamic normal load experiments, the increase of shear displacement of each upward segment followed the linearity law (Figures 9b, 9d and 9f). We suspect that this may be due to the differing mechanisms between the dynamic shear load and dynamic normal load, in that the dynamic normal stress reduced the shear resistance by decreasing the

effective normal stress. This may indicate that the vibration in the normal stress direction can more readily trigger sliding than that in the SS direction.

We noted that the slow recovery of the shear modulus after the vibration roughly follows a logarithmic law. This slowly healing was observed in other studies, where it is referred to as “slow dynamics” (Johnson & Jia, 2005), “stress relaxation” (Hartley & Behringer, 2003), or “aging effect” (Jia et al., 2011). This slow healing was also observed at the field scale (Bontemps et al., 2020; Gassenmeier et al., 2016). In our experiments, the results indicate that the changes in shear modulus not only have a function in earthquake triggering but affect the deceleration slip process after the earthquake. When the shear resistance after vibration was less than the SS, the post-vibration slip of the sample slowed down and eventually stopped. This was because the recovery of the shear modulus after vibration made the shear resistance of the sample greater than the SS. And the instability of the sample after the vibration was because the weakening amplitude of the shear modulus was large, and it was difficult to recover. This indicates that the relaxation period after the vibration is due to the recovery of the shear resistance. The shear modulus can recover to its initial value over a long enough period (Jia et al., 2011; Johnson & Jia, 2005), and the smaller the decrease of shear modulus caused by the small amplitude or short duration of the vibration, the faster it recovered to the initial value (Figure 15).

The changes of shear modulus are related to strain amplitude (Seed & Idriss, 1970), and they are affected by many macro and micro factors (Jia et al., 2011). Our dynamic triaxial-bender experimental results show that the axial strain of specimens caused by vibration was about 0.276%, 1.26%, and 2.69% respectively; the larger amplitude and longer duration caused larger strain (Figure 15). The results also show that dilation occurred during vibration (Figure 15). Thus, the macroscopic mechanisms for the weakening of the shear modulus were structure changes and particle rearrangement (Xing et al., 2021). In addition, slippage at the scale of micro-asperities under microscopic strain amplitude may also contribute to weakening (Jia et al., 2011; Johnson & Jia, 2005) because the shear modulus underwent a slight decrease while the axial strain was stable. After the vibration, the strain remained stable and the density increased slightly, and the recovery of the shear modulus may be the result of plastic creep growth of weakened contacts (Jia et al., 2011). In the dynamic normal load experiments, the volume is basically unchanged before and after vibration; the drastic volume change during the vibration process caused severe slip between the particles, which may be the main reason for the decrease of shear resistance during the vibration process. In the cyclic shear loading tests, the fluctuation of vertical displacement may indicate particle dilatancy during the shearing process; the decrease in shear resistance is the result of a combination of dilation and slippage.

4.2. Implications for Earthquake-Triggered Landslides

Our observations using monodisperse glass spheres provide insights on the effect of amplitude and duration of cyclic loading on frictional sliding instability in granular media. To further explore the influence of particle shape and size, we conducted the cyclic shear loading tests with quartz sands and polydisperse glass spheres. The polydisperse glass spheres had a lognormal particle size distribution (PSD) by weight which can represent the PSD of a mature shear band in 0.1–1.75 mm (Figure 17) (An & Sammis, 1994). The test results of the three materials are largely identical (Figures 16 and 18).

The real sliding zone materials of landslides have complex characteristics, including different particle gradations, different particle shapes, and different lithologies, and contain significant percentages of clay, which are very different from the monodisperse glass spheres or other granular materials. Although the materials used in our experiments are simplified compared to sliding zone gouges, the underlying deformation and dynamic weakening mechanisms may be similar. Because of the high control on many parameters (i.e., particle shape and size), glass spheres are widely used to study the mechanical behavior of landslide and fault gouge (Jia et al., 2011; Johnson et al., 2008, 2012, 2016; Johnson & Jia, 2005; Léopoldès et al., 2020), and are often used in DEM models. In addition, our experimental results for shear displacement have a similar trend to the displacement of the real landslide in the earthquake (Bontemps et al., 2020). The relative seismic velocity decrease caused by earthquakes in the landslide body is also similar to that of our dynamic triaxial-bender experiment (Bontemps et al., 2020). Studying the influence of other complicated factors using real landslide materials is planned in our future work.

Our experiments were carried out under dry conditions. However, in natural conditions, earthquake-triggered landslides usually involve water, especially in the process of vibration, which can produce excess pore pressure

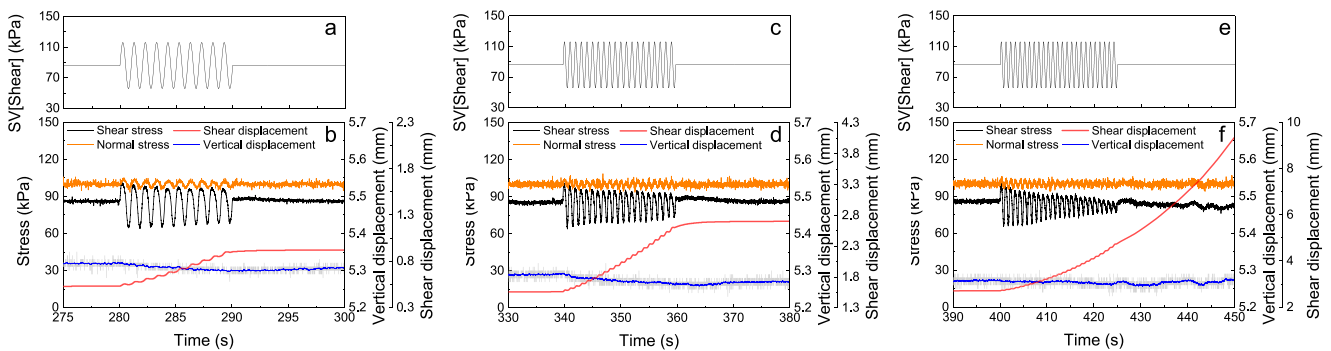


Figure 16. Cyclic shear loading tests at different numbers of cycles under 100 kPa normal stress and 86 kPa shear stress with quartz sands. (a), (c), and (e) are the graphs of the input sinusoidal dynamic load, the amplitude is 30 kPa, the frequency is 1 Hz, the number of cycles is 10, 20, and 25, respectively. (b), (d), and (f) are the graphs of experimental results, showing the change of normal stress (orange line), shear stress (black line), shear displacement (red line), and vertical displacement (blue line).

in the sliding zone. This factor can further reduce the shear resistance and induce co-seismic landslides. Strong earthquakes are known to trigger large numbers of landslides (Chigira et al., 2010; Huang & Fan, 2013; Keefer, 1984, 2002; Massey et al., 2020). In our experiments, the amplitudes of cyclic stress change from 10 to 50 kPa, and the rate of cyclic stress amplitudes to the static stresses varies from 4% to 46%. In natural conditions, the seismic ground motion would be stronger than the cyclic stress load used in the laboratory in the near field. The peak ground motion acceleration of the 2008 Mw 8.0 Wenchuan earthquake is almost 1g (Wang et al., 2013), and the peak ground motion acceleration of many strong earthquakes is above 0.5 g, such as the 1999 M 7.6 Chi-Chi earthquake in Taiwan (Wang et al., 2002), the 2011 M 9.0 Tohoku earthquake in Japan (Miyagi et al., 2011), and the 2002 M 7.9 Alaska quake (Gorum et al., 2014).

Earthquakes can also trigger landslides far from the epicenter. In the current studies, statistical analyses of earthquake-triggered landslides catalogs suggested that the maximum distance between the co-seismic landslides and the epicenter is about 500–550 km (Keefer, 1984). The ground motion decreases with the increase of the distance from the epicenter (Meunier et al., 2007), and this maximum distance indirectly represents the threshold ground motion required for the landslide to be triggered. Studies of earthquake-triggered earthquakes suggested that even a small dynamic strain amplitude of 10^{-6} can trigger earthquake thousands of kilometers away from the earthquake epicenter when the triggered fault is in a critical state (Johnson & Jia, 2005). An interesting question is raised from this topic: whether landslides can be triggered by an earthquake located thousands of kilometers away or not? We think that theoretically the landslide can be triggered by tiny fluctuations of stress. Like fault shear zone, landslides have sliding zone which controls the mechanical behaviors of landslides. The landslide sliding zone can be at a critical state, namely at the verge of failure. If this is true, the landslide shear zone at critical state can slide with tiny fluctuations of stress. However, the previous reports and statistical analysis show that most of the earthquake-induced landslides are located near the epicenter of the earthquake (within 100–200 km) and are triggered by strong motion (Dai et al., 2011; Keefer, 1984; Meunier et al., 2007). Very rare references report that the far-located landslide (thousands of kilometers away) can be triggered by earthquakes. Keefer (1984) reported an earthquake-induced (Mw 9.2 earthquake in Alaska in 1964) landslide located about 550 km away from the epicenter. We believe that the previous statistical studies focused on destructive and big earthquake-induced landslides, but ignored the correlations between the earthquake and the far-located landslide which may be triggered by the earthquake. The ignorance of earthquake-induced far located landslides can be also due to the missing of monitoring system. In addition, it is much more difficult to detect a landslide than an earthquake in mountainous areas. We think that the experimental study on the effect of tiny stress fluctuations on landslide shear zone should be carried out in the future work and the monitoring system should be enhanced to detect the earthquake-induced far-located landslide.

We conducted experiments with different vibration amplitudes to study the impact of earthquake magnitude. The results show that larger vibration amplitudes are more likely to trigger sliding (Figures 11, 12, and 13c); this was not only because the larger amplitude can provide greater driving force, but also because the larger the vibration amplitude, the greater the decrease in the shear modulus: after 200 vibration cycles, the shear modulus decreased by 3.5%, 6.45%, and 7.25% at 15 kPa, 45 kPa, and 75 kPa, respectively (Figure 15). The reduction of shear

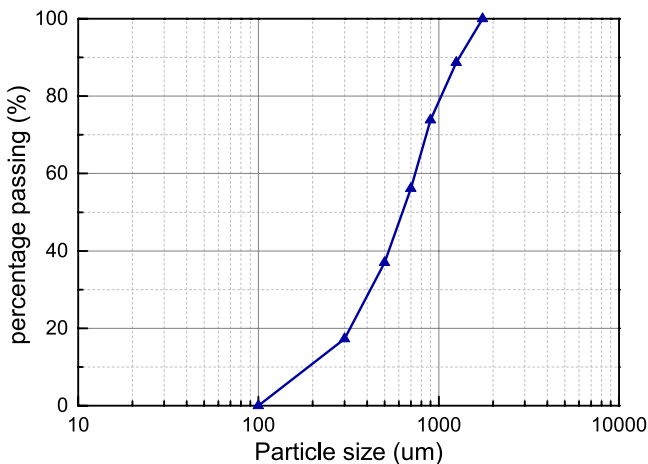


Figure 17. Particle size distribution of the polydisperse glass spheres sample.

slope body is attributed to this (Bontemps et al., 2020; Gassenmeier et al., 2016; Richter et al., 2014). Crushing will further reduce the shear resistance of the material. In our experiment, the change of shear modulus has a similar trend to the change of seismic velocity observed in the field (Bontemps et al., 2020). We suspect that these factors, including larger changes in structure and the larger amplitude of vibration and strain compared to that in the laboratory, may cause a larger reduction in shear modulus in field rather than laboratory results during earthquakes. The healing phase is attributed to the re-compaction of the soil, with the grains cementing together (Bontemps et al., 2020; Gassenmeier et al., 2016; Richter et al., 2014). We speculate that real cohesive sliding zone materials, especially when combined with precipitation, will have stronger healing capability than glass spheres.

5. Conclusion

Our dynamic ring shear experimental observations suggested that it is easier to trigger landslides with longer durations of shaking and with larger seismic wave amplitudes, and the triggering is closely related to the weakening of shear resistance. The results of dynamic triaxial-bender tests showed the decrease of shear modulus is dependent on the duration and amplitude of vibration, and the recovery of the shear modulus is dependent on the reduced amplitude of the shear modulus during vibration. The results suggest that the reduction and recovery of shear modulus is an important mechanism for triggering failure of earthquake-triggered landslides. We infer that the earthquake-induced decrease in shear modulus was caused by structure changes, particle rearrangement, and

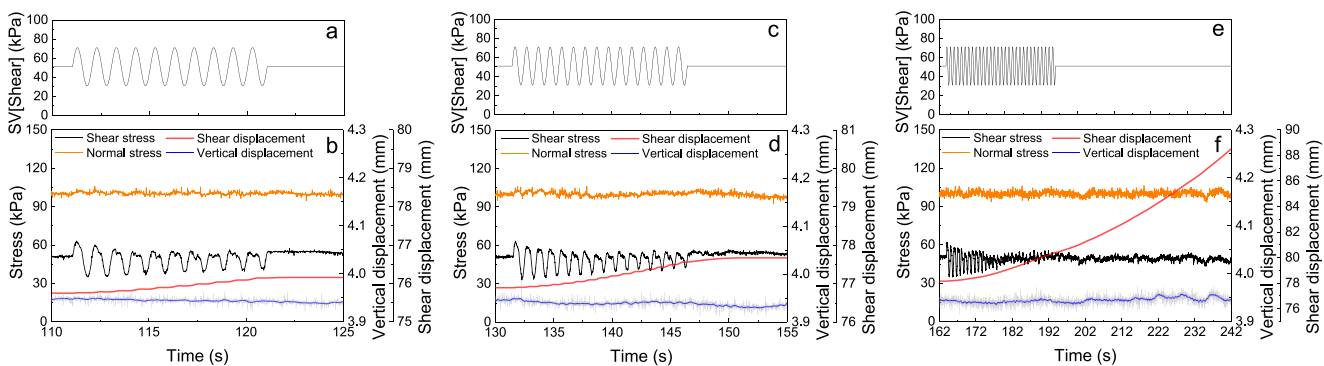


Figure 18. Cyclic shear loading tests at different numbers of cycles under 100 kPa normal stress and 51 kPa shear stress with polydisperse glass spheres. (a), (c), and (e) are the graphs of the input sinusoidal dynamic load, the amplitude is 20 kPa, the frequency is 1 Hz, the number of cycles is 10, 15, and 30, respectively. (b), (d), and (f) are the graphs of experimental results, showing the change of normal stress (orange line), shear stress (black line), shear displacement (red line), and vertical displacement (blue line).

modulus was affected by the combination of vibration amplitude and duration (Seed & Idriss, 1970). We noted that vibration with a small amplitude for a long duration could cause a greater weakening of shear modulus than vibration with a large amplitude for a short duration. As shown in Figure 15c point A and point B, under the same stress conditions, the vibration with amplitude of 45 kPa and 49 vibration cycles caused 4% weakening of the shear modulus, while the vibration with amplitude of 75 kPa and six vibration cycles caused 3.8% weakening of the shear modulus. This is consistent with instances in which some earthquakes with a small magnitude but a long duration caused more co-seismic landslides than earthquakes with a large magnitude and a short duration (Jibson et al., 2020b). When the number of vibration cycles is the same, the larger amplitude caused larger strain and shear modulus weakening. This also explains why earthquakes with larger magnitudes and longer durations can be extremely destructive, such as the 2008 Wenchuan earthquake (Jibson & Tanyaş, 2020).

In the laboratory, glass spheres were not broken. However, in natural conditions, damage to the soil and fracturing of the rock mass was observed in the sliding zones and slope bodies, and the reduction of seismic velocity in the

slipping at the scale of micro-asperities. Our results suggested how earthquakes with larger seismic wave amplitudes and long durations can trigger more co-seismic landslides.

Data Availability Statement

All the original data used in this work can be retrieved from the data set available (in the link: <https://doi.org/10.6084/m9.figshare.21221750.v1>).

Acknowledgments

We are supported by National Basic Research Program of China: basic research fund (42090051), the funds for creative research groups of Sichuan Province (2021JDTD0014).

References

- An, L. J., & Sammis, C. G. (1994). Particle size distribution of cataclastic fault materials from southern California: A 3-D study. *Pure and Applied Geophysics*, 143(1), 203–227. <https://doi.org/10.1007/bf00874329>
- Bontemps, N., Lacroix, P., Larose, E., Jara, J., & Taipe, E. (2020). Rain and small earthquakes maintain a slow-moving landslide in a persistent critical state. *Nature Communications*, 11(1), 780. <https://doi.org/10.1038/s41467-020-14445-3>
- Chigira, M., Wu, X., Inokuchi, T., & Wang, G. (2010). Landslides induced by the 2008 Wenchuan earthquake, Sichuan, China. *Geomorphology*, 118(3–4), 225–238. <https://doi.org/10.1016/j.geomorph.2010.01.003>
- Clayton, C. R. I. (2011). Stiffness at small strain: Research and practice. *Géotechnique*, 61(1), 5–37. <https://doi.org/10.1680/geot.2011.61.1.5>
- Cui, S. H., Wang, G. H., Pei, X. J., Huang, R. Q., & Kamai, T. (2016). On the initiation and movement mechanisms of a catastrophic landslide triggered by the 2008 Wenchuan (M_s 8.0) earthquake in the epicenter area. *Landslides*, 14(3), 1–819. <https://doi.org/10.1007/s10346-016-0754-y>
- Dai, F. C., Xu, C., Yao, X., Xu, L., Tu, X. B., & Gong, Q. M. (2011). Spatial distribution of landslides triggered by the 2008 Ms 8.0 Wenchuan earthquake, China. *Journal of Asian Earth Sciences*, 40(4), 883–895. <https://doi.org/10.1016/j.jseas.2010.04.010>
- Delgado, J., Garrido, J., López-Casado, C., Martino, S., & Peláez, J. A. (2011). On far field occurrence of seismically induced landslides. *Engineering Geology*, 123(3), 204–213. <https://doi.org/10.1016/j.enggeo.2011.08.002>
- Gassenmeier, M., Sens-Schönfelder, C., Eulenfeld, T., Bartsch, M., Victor, P., Tilmann, F., & Korn, M. (2016). Field observations of seismic velocity changes caused by shaking-induced damage and healing due to mesoscopic nonlinearity. *Geophysical Journal International*, 204(3), 1490–1502. <https://doi.org/10.1093/gji/ggv529>
- Gorum, T., Korup, O., Van Westen, C. J., Van der Meijde, M., Xu, C., & Van der Meer, F. D. (2014). Why so few? Landslides triggered by the 2002 Denali earthquake, Alaska. *Quaternary Science Reviews*, 95, 80–94. <https://doi.org/10.1016/j.quascirev.2014.04.032>
- Hartley, R. R., & Behringer, R. P. (2003). Logarithmic rate dependence of force networks in sheared granular materials. *Nature*, 421(6926), 928–931. <https://doi.org/10.1038/nature01394>
- Huang, R. Q., & Fan, X. M. (2013). The landslide story. *Nature GeoScience*, 6(5), 325–326. <https://doi.org/10.1038/ngeo1806>
- Indraratna, B., Tennakoon, N., Nimbalkar, S., & Rujikiatkamjorn, C. (2013). Behaviour of clay-fouled ballast under drained triaxial testing. *Géotechnique*, 63(5), 410–419. <https://doi.org/10.1680/geot.11.p.086>
- Jia, X. P., Brunet, T., & Laurent, J. (2011). Elastic weakening of a dense granular pack by acoustic fluidization: Slipping, compaction, and aging. *Physical Review E: Statistical, Nonlinear, and Soft Matter Physics*, 84(2), 020301. <https://doi.org/10.1103/physreve.84.020301>
- Jibson, R. W., Grant, A. R. R., Witter, R. C., Allstadt, K. E., Thompson, E. M., & Bender, A. M. (2020). Ground failure from the anchorage, Alaska, earthquake of 30 November 2018. *Seismological Research Letters*, 91(1), 19–32. <https://doi.org/10.1785/0220190187>
- Jibson, R. W., & Tanyas, H. (2020). The influence of frequency and duration of seismic ground motion on the size of triggered landslides—A regional view. *Engineering Geology*, 273, 105671. <https://doi.org/10.1016/j.enggeo.2020.105671>
- Johnson, P. A., Carmeliet, J., Savage, H. M., Scuderi, M., Marone, C., Guyer, R. A., et al. (2016). Dynamically triggered slip leading to sustained fault gouge weakening under laboratory shear conditions. *Geophysical Research Letters*, 43(4). <https://doi.org/10.1002/2015gl067056>
- Johnson, P. A., Carpenter, B., Knuth, M., Kaproth, B., Le Bas, P., Daub, E., & Marone, C. (2012). Nonlinear dynamical triggering of slow slip on simulated earthquake faults with implications to Earth. *Journal of Geophysical Research*, 117(B4), B04310. <https://doi.org/10.1029/2011JB008594>
- Johnson, P. A., & Jia, X. P. (2005). Nonlinear dynamics, granular media and dynamic earthquake triggering. *Nature*, 437(7060), 871–874. <https://doi.org/10.1038/nature04015>
- Johnson, P. A., Savage, H., Knuth, M., Gomberg, J., & Marone, C. (2008). The effect of acoustic waves on stick-slip behavior in sheared granular media: Implications for earthquake recurrence and triggering. *Nature*, 451(7174), 57–60. <https://doi.org/10.1038/nature06440>
- Keefer, D. K. (1984). Landslides caused by earthquakes. *The Geological Society of America Bulletin*, 95(4), 406–421. [https://doi.org/10.1130/0016-7606\(1984\)95<406:lcbe>2.0.co;2](https://doi.org/10.1130/0016-7606(1984)95<406:lcbe>2.0.co;2)
- Keefer, D. K. (2002). Investigating landslides caused by earthquakes—A historical review. *Surveys in Geophysics*, 23(6), 473–510. <https://doi.org/10.1023/a:1021274710840>
- Lacroix, P., Perfettini, H., Taipe, E., & Guillier, B. (2014). Co- and Postseismic motion of a landslide; observations, modelling and analogy with tectonic faults. *Geophysical Research Letters*, 41(19), 6676–6680. <https://doi.org/10.1002/2014GL061170>
- Léopoldès, J., Jia, X. P., Tourin, A., & Mangeney, A. (2020). Triggering granular avalanches with ultrasound. *Physical Review E*, 102(4), 042901. <https://doi.org/10.1103/physreve.102.042901>
- Lin, W. L., Liu, A., & Mao, W. W. (2019). Use of acoustic emission to evaluate the micro-mechanical behavior of sands in single particle compression tests. *Ultrasonics*, 99, 105962. <https://doi.org/10.1016/j.ultras.2019.105962>
- Malamud, B. D., Turcotte, D. L., Guzzetti, F., & Reichenbach, P. (2004). Landslides, earthquakes, and erosion. *Earth and Planetary Science Letters*, 229(1–2), 45–59. <https://doi.org/10.1016/j.epsl.2004.10.018>
- Mao, W. W., Yang, Y., Lin, W. L., Aoyama, S., & Towhata, I. (2018). High frequency acoustic emissions observed during model pile penetration in sand and implications for particle breakage behavior. *International Journal of Geomechanics*, 18(11). [https://doi.org/10.1061/\(ASCE\)GM.1943-5622.0001287](https://doi.org/10.1061/(ASCE)GM.1943-5622.0001287)
- Martha, T. R., Roy, P., Mazumdar, R., Govindhara, K. B., & Kumar, K. V. (2016). Spatial characteristics of landslides triggered by the 2015 Mw 7.8 (Gorkha) and Mw 7.3 (Dolakha) earthquakes in Nepal. *Landslides*, 14(2), 1–704. <https://doi.org/10.1007/s10346-016-0763-x>
- Massey, C. I., Townsend, D., Jones, K., Lukovic, B., Rhoades, D., Morgenstern, R., et al. (2020). Volume characteristics of landslides triggered by the M_w 7.8 2016 Kaikōura Earthquake, New Zealand, derived from digital surface difference modeling. *Journal of Geophysical Research: Earth Surface*, 125(7), e2019JF005163. <https://doi.org/10.1029/2019jf005163>

- Meunier, P., Hovius, N., & Haines, A. J. (2007). Regional patterns of earthquake-triggered landslides and their relation to ground motion. *Geophysical Research Letters*, 34(20), L20408. <https://doi.org/10.1029/2007GL031337>
- Meunier, P., Hovius, N., & Haines, A. J. (2008). Topographic site effects and the location of earthquake induced landslides. *Earth and Planetary Science Letters*, 275(3–4), 221–232. <https://doi.org/10.1016/j.epsl.2008.07.020>
- Michlmayr, G., & Cohen, D. (2014). Mechanisms for acoustic emissions generation during granular shearing. *Granular Matter*, 16(5), 627–640. <https://doi.org/10.1007/s10035-014-0516-2>
- Miyagi, T., Higaki, D., Yagi, H., Doshida, S., Chiba, N., Umemura, J., & Satoh, G. (2011). Reconnaissance report on landslide disasters in northeast Japan following the M 9 Tohoku earthquake. *Landslides*, 8(3), 339–342. <https://doi.org/10.1007/s10346-011-0281-9>
- Newmark, N. M. (1965). Effects of earthquakes on dams and embankments. *Géotechnique*, 15(2), 139–160. <https://doi.org/10.1680/geot.1965.15.2.139>
- Papazachos, B. C., Tsapanos, T. M., & Panagiotopoulos, D. G. (1982). A premonitory pattern of earthquakes in northern Greece. *Nature*, 296(5854), 232–235. <https://doi.org/10.1038/296232a0>
- Richter, T., Sens-Schönfelder, C., Kind, R., & Asch, G. (2014). Comprehensive observation and modeling of earthquake and temperature-related seismic velocity changes in northern Chile with passive image interferometry. *Journal of Geophysical Research: Solid Earth*, 119(6), 4747–4765. <https://doi.org/10.1002/2013jb010695>
- Sassa, K., Fukuoka, H., Wang, F., & Wang, G. H. (2007). In K. Sassa, H. Fukuoka, F. Wang, & G. Wang (Eds.), *Progress in landslide science*, 193–207. Springer Berlin Heidelberg.
- Sassa, K., Fukuoka, H., Wang, G. H., & Ishikawa, N. (2004). Undrained dynamic-loading ring-shear apparatus and its application to landslide dynamics. *Landslides*, 1, 7–19. <https://doi.org/10.1007/s10346-003-0004-y>
- Seed, H. B., & Idriss, I. M. (1970). Soil moduli and damping factors for dynamic response analyses.
- Shirley, D. J., & Hampton, L. D. (1978). Shear wave measurements in laboratory sediments. *Journal of Acoustical Society of America*, 63(2), 607–613. <https://doi.org/10.1121/1.381760>
- Trifunac, M. D. (2008). Energy of strong motion at earthquake source. *Soil Dynamics and Earthquake Engineering*, 28(1), 1–6. <https://doi.org/10.1016/j.soildyn.2007.06.009>
- Wang, G. H., Huang, R. Q., Chigira, M., Wu, X. Y., & Lourenço, S. D. N. (2013). Landslide amplification by liquefaction of runout-path material after the 2008 Wenchuan (M 8.0) earthquake, China. *Earth Surface Processes and Landforms*, 38(3), 265–274. <https://doi.org/10.1002/esp.3277>
- Wang, G. H., Huang, R. Q., Lourenço, S. D. N., & Kamai, T. (2014). A large landslide triggered by the 2008 Wenchuan (M 8.0) earthquake in Donghekou area: Phenomena and mechanisms. *Engineering Geology*, 182, 148–157. Part B(0). <https://doi.org/10.1016/j.enggeo.2014.07.013>
- Wang, G. H., Suemine, A., Zhang, F. Y., Hata, Y., Fukuoka, H., & Kamai, T. (2014). Some fluidized landslides triggered by the 2011 Tohoku earthquake (Mw 9.0), Japan. *Geomorphology*, 208, 11–21. <https://doi.org/10.1016/j.geomorph.2013.11.009>
- Wang, S. J. (1977). Preliminary notes on the dynamic stability of rock slopes. *Scientia Geologica Sinica*(04), 372–376.
- Wang, S. J., & Zhang, J. M. (1982). On the dynamic stability of block sliding on rock slopes. *Scientia Geologica Sinica*(02), 162–170.
- Wang, W. N., Nakamura, H., Tsuchiya, S., & Chen, C. C. (2002). Distributions of landslides triggered by the Chi-chi earthquake in Central Taiwan on September 21, 1999. *Landslides*, 38(4), 318–326. https://doi.org/10.3313/jls1964.38.4_318
- Xing, Y., Zheng, J., Li, J., Cao, Y., Pan, W., Zhang, J., & Wang, Y. (2021). X-ray tomography investigation of cyclically sheared granular materials. *Physical Review Letters*, 126(4), 048002. <https://doi.org/10.1103/physrevlett.126.048002>
- Xu, Q., Shang, Y., Van Asch, T., Wang, S., Zhang, Z., & Dong, X. (2012). Observations from the large, rapid Yigong rock slide-debris avalanche, southeast Tibet. *Canadian Geotechnical Journal*, 49(5), 589–606. <https://doi.org/10.1139/t2012-021>
- Zhou, Y. G., & Chen, Y. M. (2005). Influence of seismic cyclic loading history on small strain shear modulus of saturated sands. *Soil Dynamics and Earthquake Engineering*, 25(5), 341–353. <https://doi.org/10.1016/j.soildyn.2005.03.001>